Comparison of rib bone surrogates from additive manufacturing, cast material and PMHS data under dynamic loading

Marcin Jenerowicz, Thomas Haase, Markus Linnenberg, Klaus Hoschke,
Matthias Boljen, Stefan Hiermaier

Abstract The objective of this study is to evaluate different rib bone surrogates by comparing them to specific, male PMHS data from Charpail *et al.* (2005), Kindig (2009), Agnew *et al.* (2018) and Kang *et al.* (2020). The Fraunhofer EMI 5th male rib surrogates were fabricated from Scalmalloy® (AlMg4.5Sc0.7Zr0.3) using additive manufacturing. The CTS PRIMUS breakable dummy from *Crashtest-Service-Dummy-Solution GmbH* is already being used as an anthropomorphic test device (ATD) in various areas. Its cast 5th left rib, constructed from a mixture of epoxy resin and aluminium powder, was also included in this study. A test setting based on the setup of Charpail *et al*. (2005) was developed. The specimens were dynamically (500 mm/s) loaded to failure in a bending scenario imitating a frontal thoracic impact. During the tests, not only force and displacement were measured, but also the strain distribution using 3D digital image correlation (3D-DIC) and compared to PMHS data of the previously mentioned studies. Both rib surrogates show strong deviations from the PMHS characteristic values. Nevertheless, there are also common characteristics in key variables to certain age groups of the PMHS data. The differences shown are an important contribution to the further development and improvement of both surrogates.

Keywords Additive manufacturing, Cast materials, Digital image correlation, PMHS data, Rib bone surrogates.

I. INTRODUCTION

Despite significant advances in the development of passive and active crash protection components, thoracic injuries, particularly rib fractures, are still the most common type of injury to occupants in motor vehicle collisions [1-3]. This is due to the high loads imposed on the rib cage during impact [4-6]. A study from the field of injury prevention states that the reduction in injury risk due to advances in vehicle safety technology and assessment methods has less impact on the chest compared to other body regions [7]. One uncertainty of this statement is whether this obstruction in reducing thoracic injury risk is due to inadequacies in assessment methods or to the increasing vulnerability of vehicle occupants resulting from an increasing shift in age demographics [7]. In particular, rib fractures and soft tissue injuries to the thorax, such as pulmonary contusions, remain a leading cause of death [8-10] and are considered indicators of the severity of trauma in the elderly, as mortality rates increase with advancing age [1][11-12]. The material properties of cortical bone change dramatically with advancing age [13-15]. Nevertheless, age alone is not the only important factor that influences material properties. Numerous studies demonstrate that sex, body size, body mass index (BMI), cortical cross-sectional thickness [13][15-20] and the often-neglected strain rate dependence of the compact bone tissue [21-22] are also exceedingly important.

Several studies have been carried out on the local characterization of ribs [19][23-28], but they are limited to specific areas and do not provide an accurate description for every point of the thorax. The complexity of characterizing rib geometry lies in defining relatively thin and irregular zones and representing this complex structure of trabecular and cortical bone. One study analyzed, through the application of new techniques (multi-scale imaging techniques), the definition of local measures, such as cross-sectional areas, percentage of cortical

M. Jenerowicz (e-mail: marcin.jenerowicz@emi.fraunhofer.de; tel: +49-761-2714-359) is a research fellow at the Fraunhofer Institute for High-Speed Dynamics, Ernst-Mach-Institut (EMI), and a PhD candidate at the Faculty of Engineering of the Albert-Ludwigs-University in Freiburg, Germany. S. Hiermaier is Professor for Sustainable Systems Engineering at the Faculty of Engineering of the Albert-Ludwigs-University and the Director of the Fraunhofer Institute for High-Speed Dynamics, EMI. T. Haase, M. Linnenberg, K. Hoschke and M. Boljen are affiliated with the Fraunhofer Institute for High-Speed Dynamics, EMI.

and trabecular bone, moment of inertia of the cross-section and variations in cortical bone thickness at different locations [16]. This study presents the stated material properties and parameters of all ribs over the whole rib curve length of the whole thorax of 18 PMHS in rib levels 1 to 10.

Anthropomorphic test devices (ATDs) are typically manufactured for standardized crash tests where reproducible measurements are required for a specific load and impact direction. The impact directions and velocities are predefined, so the dummies that are used can only be applied to nearly similar configurations and loads [29-30]. Therefore, a new dummy (CTS PRIMUS breakable) was developed in a consortium of accident research institutions – *Crashtest-Service-Dummy-Solution GmbH* (CTS), *Priester & Weyde* (P&W) and the *Dresden University of Applied Sciences* (HTW) – to obtain realistic results in forensic accident reconstruction [31-33]. The goal was to develop a human mid-sized male surrogate capable of providing authentic vehicle damage as well as damage to its own structural components, allowing to find a match between dummy damage and injury probability. Thus far, however, only validation tests in crash domain have been performed, representing the validity and the global structural behaviour (trajectory, damage to internal and external structures) of the dummy for specific accident outcomes [34]. The aim of the present study is to present the direct comparison of 5th left rib surrogates of the CTS PRIMUS breakable dummy (referred to as CTS rib in the following) to material properties from PMHS data in the literature [19][24][26][28] in order to improve the evaluation of the validation of the individual structures.

Additive manufacturing has been used for years in the fabrication of prostheses and bone replacement structures [35-37]. The advantages of this manufacturing method include high precision and direct adjustability of material properties by varying the processing parameters, as well as biological compatibility [36][38]. At the *Fraunhofer Institute for High-Speed Dynamics, Ernst-Mach-Institut* (EMI), additive manufacturing has already been applied in many fields of application, such as topology optimization of aerospace structural components [39-40]. In the present study, additive manufacturing was used to fabricate a geometrically realistic rib bone surrogate of the left 5th male human rib (referred to as EMI rib in the following) and to provide a direct comparison to the CTS rib and to material properties from PMHS data in the literature [19][24][26][28].

II. METHODS

The PMHS experimental data from literature [19][24][26][28] were extensively reprocessed. Where possible, only data from male 22+ year old subjects and the 5th rib were used to provide a suitable data set for comparison to the surrogates. The following metrics were used: peak force, *x*-displacement, peak displacement, peak strain @60% Cv.Le, and stiffness *K* (slope of a line 20-80 % of linear portion of force-displacement (F-D) curve). Additionally, an investigation of the effect of load rate on the CTS surrogate rib response was performed, as the material has shown strain rate dependence in preceding tests at EMI (Table I).

Materials

The bones of the CTS PRIMUS breakable dummy are made of a multi-component cast material [32]. Specifically, it is a mixture of epoxy resin and aluminium powder. The exact mixing ratio is known only to the manufacturer and developer. Prior investigations (quasi static and dynamic tensile tests) at EMI on sample plates, which were made by CTS under the same manufacturing conditions as the bone surrogates, have determined the following material properties, which are shown in Table I (no further publication of the data is available).

TABLE I
DETERMINED MATERIAL PARAMETERS FOR THE BONE SURROGATE OF THE CTS PRIMUS BREAKABLE DUMMY

	Units	Measured Value	Standard Deviation
Material density	g/cm^3	1.37	0.006
Young's modulus	GPa	5.50	0.26
Tensile strength (0.01/s)	MPa	42.30	1.15
Tensile strength (1.0/s)	MPa	52.40	2.78
Elongation at break (0.01/s)	%	1.11	0.06
Elongation at break (1.0/s)	%	1.34	0.09

In order to determine any strain rate dependency, the uniaxial tensile strength tests were carried out at two strain rates (0.01/s, 1.0/s). The dependency was clearly identified. Therefore, the CTS ribs were also tested at further load rates (2 mm/s, 500 mm/s) to identify the influence on the structural properties.

The material for the rib surrogates manufactured at EMI is the Scalmalloy® AlMg4.5Sc0.7Zr0.3 (supplier Heraeus; powder particle size distribution (PSD) measured to D_{10}: 20.1 µm; D_{50}: 36.1 µm and D_{90}: 53.7 µm with a Camsizer X2). The main material properties are summarized in Table II. The production parameters, such as laser power, scanning speed and distance between laser tracks (hatching), and different exposure strategies with the evolving macro- and microstructures significantly influence the material properties [40-41]. In the present study, only one set of the manufacturing parameters is presented. All other influencing variables were investigated in a separate research study. The strain rate sensitivity has been studied on samples manufactured by the same machine in [42]. The material Scalmalloy® shows a marginal positive strain rate dependence (ultimate tensile strength decreases weakly; yield strength remains constant), therefore only dynamic tests with the EMI ribs are performed.

TABLE II
MATERIAL PROPERTIES FOR THE SCALMALLOY® [43]

	Units	**Value**
Material density	g/cm^3	2.67
Young's modulus	GPa	70
Yield strength	MPa	470
Ultimate tensile strength	MPa	520
Elongation at break	%	13
Vickers hardness	HV0.3	180

Model Development

Since 2010, the engineering office *Priester & Weyde*, in cooperation with the Institute of Forensic Medicine at the *Charité Berlin*, as well as researchers from the *TU Berlin*, the *HTW Dresden* and the *University of Zilina*, have been continuously developing a dummy, which is used as a surrogate for individuals hit by cars in forensic re-enactments of car/pedestrian and car/cyclist collisions [44]. For a detailed description of the development and manufacturing process, please refer to the following literature [31-33].

Due to the fact that the material properties of the CTS ribs depend mainly on the mixing ratio of epoxy resin to aluminium powder, the geometric accuracy of the rib structures is only partially given. The homogeneous distribution of the mixture during the casting process implies a change in the actual geometry to realize the required fracture properties. This means that the cross-sectional areas do not match those of a real rib. At EMI, the approach is to adopt the geometry of the human rib on a 1:1 basis. As a template, the 5th rib from the GHBMC-M50 v1.5.0 model [45-46] was extracted and the outer contour was transferred to a CAD model. In the next step, the model was divided into 30 sections. Based on research work at the *Université de Valenciennes* [16], a map of the cortical bone thickness of the 5th rib was created, representing a comparable M50 percentile PMHS. These include the corresponding thicknesses of the cutaneous and pleural surfaces as well as those in the transition areas over the entire rib curve length (Cv.Le). Each section of the CAD model consists of two B-spline curves with at least 15 points through which the thickness was adopted from the table. The finished model was prepared for additive manufacturing.

In this study, a commercial *Laser Beam Melting* (LBM) machine *EOS M 400* equipped with a 1 kW laser source (YLR-Series, 1070 nm wavelength) was used to build the test specimens with the following building specifications: hatch 0.17 mm, speed 927 mm/s, power 320 W, beam offset 0.1 mm. Figures 1 and 2 illustrate the two rib surrogates side by side and Table III provides a list of the specific geometric characteristics (Cv.Le: curve length of rib from head to sternal end, Sp.Le: span length from center of vertebral end to center of sternal end, *y*-Dist.: largest distance from *x*-axis to surface of cutaneous cortex) with comparative values from PMHS investigations [19][24][26][28].

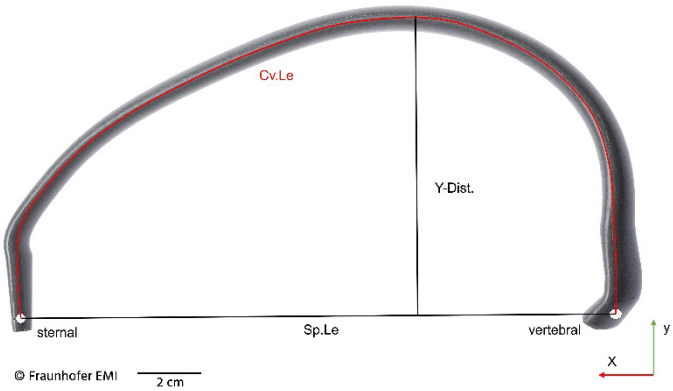

Fig. 1. 5th rib from CTS PRIMUS breakable dummy, including global geometry, vertebral end (head) is to the right and sternal end is to the left.

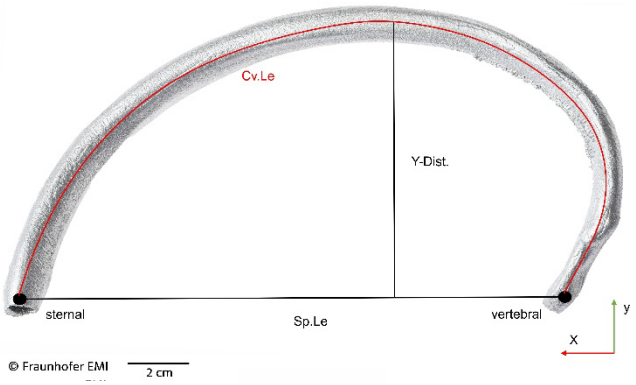

Fig. 2. EMI 5th rib from additive manufacturing, including global geometry, vertebral end (head) is to the right and sternal end is to the left.

TABLE III
RIB SURROGATES VS. PMHS GEOMETRIC PARAMETERS

	Cv.Le (mm)	**Sp.Le (mm)**	***y*-Dist. (mm)**
CTS	340	197	65
EMI	326	177	88
PMHS male 5th rib [24]	N/A	201.0 ± 15.7	N/A
PMHS male 5th rib [26]	317.5 ± 15.9	190.6 ± 14.5	93.6 ± 8.1
PMHS mid-size male 4th-7th rib lv. [28]	303.8 ± 23.4	215.7 ± 19.5	76.4 ± 8.7
PMHS 3th-8th rib lv. [19]	289.4 ± 30.2	204.1 ± 24.0	72.8 ± 9.6

Experimental Testing

To prepare for testing, the cleaned rib surrogates were potted in aluminium tubes (d = 30 mm, h = 30 mm) with Resinpal 1818 polyurethane casting resin. The vertebral and sternal ends of the surrogates were centred in the tubes, which were oriented perpendicular in the load direction to the specimen. During the potting procedure, the long axis of the specimen was restricted to a single plane.

A custom specimen fixture was developed to allow testing of different rib geometries in the same testing machine. The objective was to align the force transmission with the test devices used in the literature, the impact pendulum systems [19][24][26][47]. The test rig drove the sternal end of the specimen towards the vertebral end (displacement along the x-axis) in a simplified bending scenario mimicking a frontal thoracic impact [6]. The potted specimens were rigidly attached to the fixture. The sternal end was allowed to freely rotate around the primary bending z-axis. The vertebral end was fixed in all directions. Compressive tests (Figure 3) for the load rates quasi-static (q-s.: 2 mm/s) and dynamic (dyn.: 500 mm/s) were performed using a servo-hydraulic testing machine (Instron 8872) equipped with a 10 kN load cell (Dynacell). Testing was performed in displacement-controlled mode with constant cross-head velocities. Specimen strain was evaluated using three-dimensional digital image correlation (3D-DIC, GOM Correlate software) with a resolution of 10 pixel/mm for quasi-static and 5 pixel/mm for the dynamic tests. A fine speckle pattern with approximate speckle sizes of 0.1 mm was produced with an airbrush gun. Deformation images were recorded using the high-speed cameras Basler Cam ace-Series with 1000 × 2048 resolution at 10 fps for the quasi-static and Photron FASTCAM NOVA with 768 × 1024 resolution at 3000 fps for the dynamic tests. Due to the one-sided measurement of the 3D-DIC system, the tests for the front and back of the specimens were performed individually. Each test series had at least three valid runs. The sample size conducted is summarized in Table IV.

TABLE IV
NUMBER OF SPECIMENS TESTED

	CTS		**EMI**	
	Front	**Back**	**Front**	**Back**
Quasi-static tests (2 mm/s)	3	3	0	0
Dynamic tests (500 mm/s)	3	3	3	3

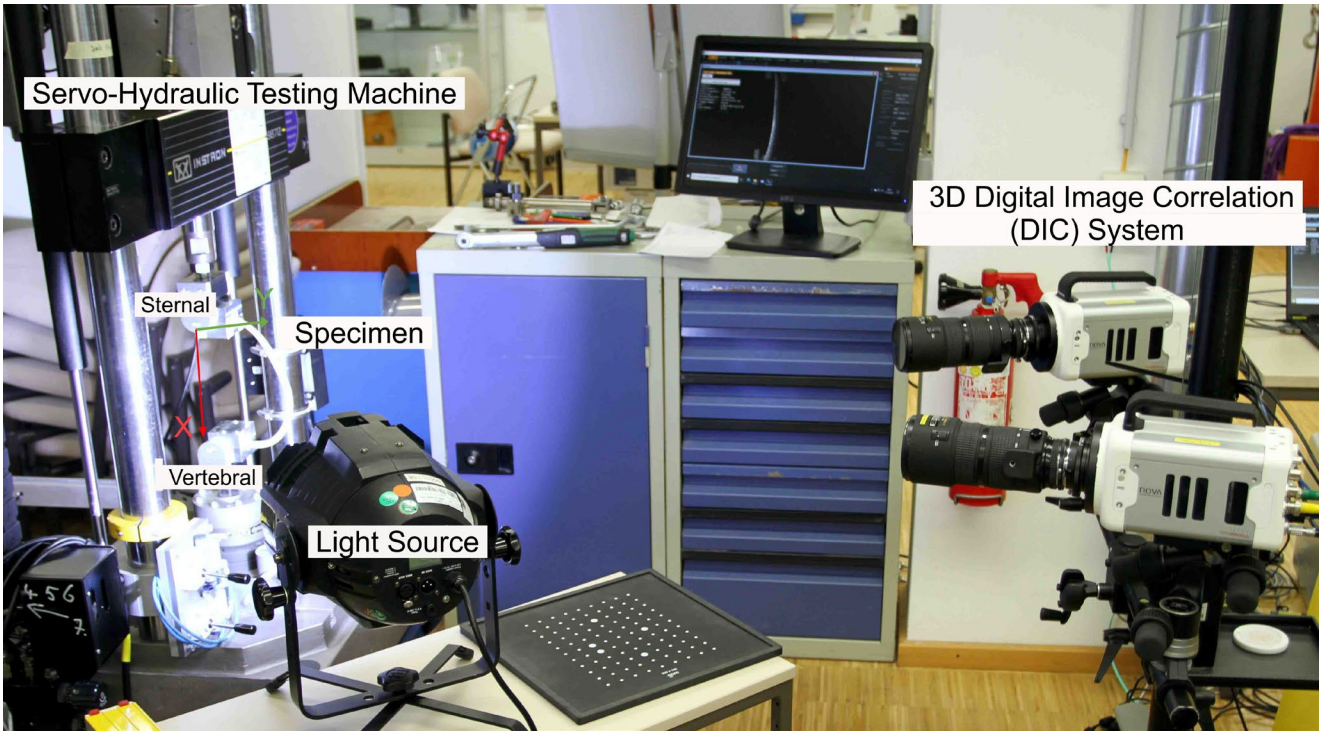

Fig. 3. Experimental setup with CTS rib in fixture and location of instrumentation. The primary orientation of loading is in *x*-direction, where the sternal end is moved towards the vertebral end by the test piston.

III. RESULTS

Figures 4 and 5 show an example of the evaluation section of the 3D-DIC system. Figure 4 presents the strain field of the CTS specimen CH03-01 for evaluation over the visible surface and Figure 5 the equal for the EMI specimen CH40-04. In PMHS tests, it is common to measure the strains at 30 % and 60 % of the Cv.Le with conventional strain gauges [19][24], so these points were explicitly marked for evaluation. Here, the advantage of the 3D-DIC becomes apparent, as it allows to determine the strains also directly at the fracture edge. In addition, it is possible to determine the location of the locally largest strain. For the evaluation, a curve was placed over the centre region of the specimens, representing the strains over the visible region of the specimen along the Cv.Le (Figure 9). As indicated earlier, the CTS specimens are quite different in cross-section from a real rib. The specimens are much flatter and wider, which results in a different strain field across the surface. The maximum strain is reached at ~65 % Cv.Le and results in a brittle fracture behaviour with about (1.91 ± 0.07) % strain. It was found that 40 % of the specimens failed in this region. The remaining specimens fractured at the restraint in the vertebral end.

The specimens fabricated at EMI show a significant strain increase in the region of ~75 % Cv.Le. This is due to the fact that the cross-sectional thickness in the pleural region is significantly higher than in the transitional regions and the cutaneous side. In addition, starting from the vertebral end, the thickness of the cortical bone reaches the local maximum at ~41 % and decreases continuously toward the sternal end until it reaches its minimum at ~70 % Cv.Le. This results in the region of maximum strains of the EMI specimens. As the Scalmalloy® material exhibits a rather plastic and ductile failure behaviour at low wall thicknesses (0.38–1.18 mm), necking occurs at the location at ~72 % Cv.Le at (0.99 ± 0.10) % strain. This was the case for all EMI specimens without exception.

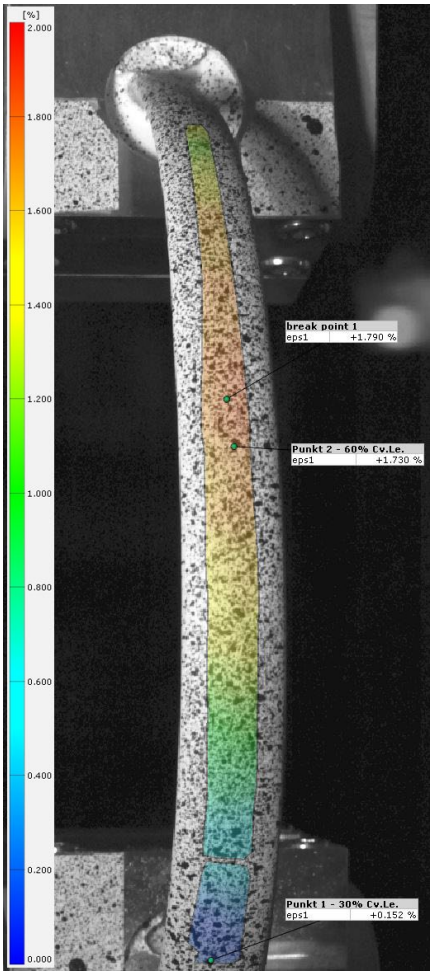

Fig. 4. Exemplary 3D-DIC of engineering strain of CTS specimen CH03-01 for determination of strain field over the visible surface. The specimen is breaking at 1.87 % strain at ~65 % of Cv.Le.

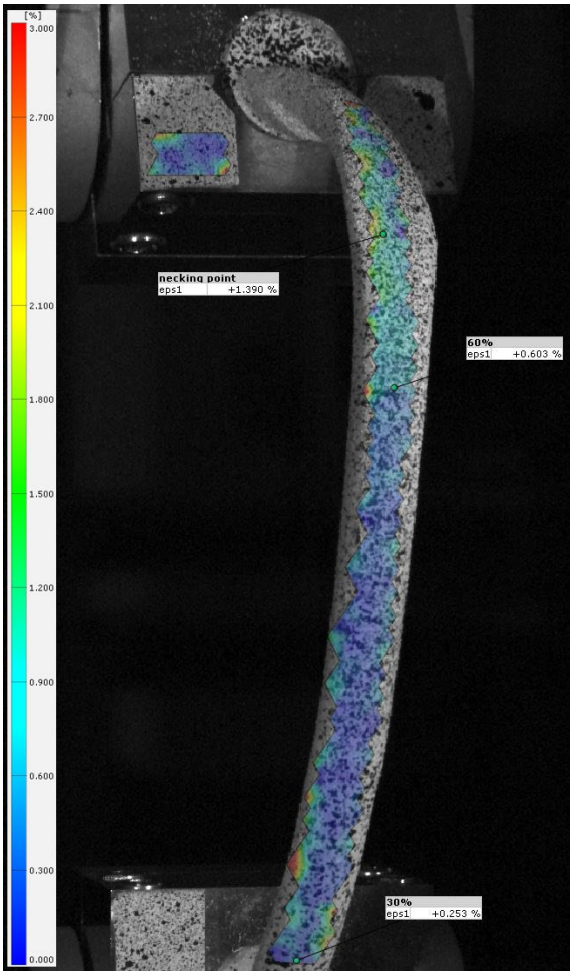

Fig. 5. Exemplary 3D-DIC of engineering strain of EMI specimen CH40-04 for determination of strain field over the visible surface. The specimen is building a necking point at 1.39 % strain at ~80 % of Cv.Le.

The average strain rates (1/s) were determined using the slopes of the fitted first order polynomial of the peak strain-time history curves on the cutaneous side of the specimen. A rotation of the mount around the *z*-axis at the sternal end was observed simultaneously with the change in strain rate of the CTS specimen. Therefore, the slopes were determined at two different ranges (30-50 % and 70-90 %) of the peak strain. Figure 6 shows the range as an example for CTS specimen CH03-01. The strain-time history of the EMI specimens indicates a linear-elastic and plastic range. The strain rates were determined using the slopes of the fitted first-order polynomial in the linear-elastic range 30-70 %. Figure 7 shows an example of the range for EMI specimen CH40-04. The curve progression of the EMI specimens is significantly more erratic because the analysis area is significantly reduced due to the smaller width of the specimens, and the quality of the speckle pattern has a considerably greater influence on the evaluation. The determined strain rates for all surrogates are summarized in Table V. The strain rate for the dynamic tests in the first range of the CTS specimens is equivalent to one of the EMI specimens.

TABLE V
DETERMINED LINEARIZED STRAIN RATES FOR RIB BONE SURROGATES

	CTS		**EMI**
	Slope 1 (10^{-2}/s)	**Slope 2 (10^{-2}/s)**	**Slope (10^{-2}/s)**
Quasi-static tests (2 mm/s)	0.049 ± 0.002	0.11 ± 0.03	N/A
Dynamic tests (500 mm/s)	12.9 ± 0.19	35.9 ± 0.18	13.8 ± 1.01

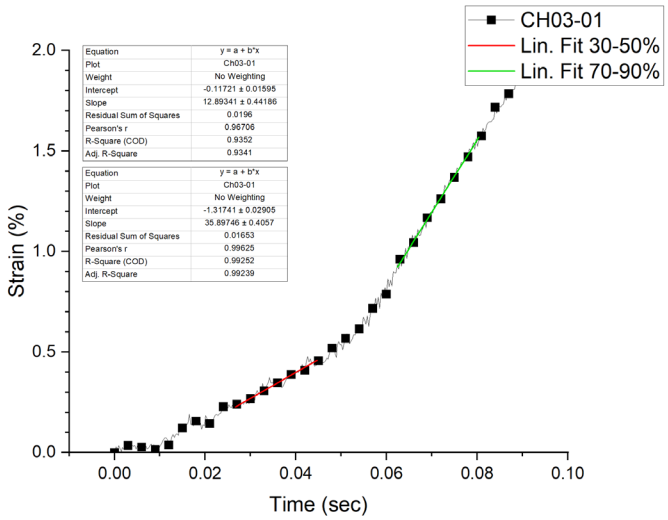

Fig. 6. Exemplary strain-time history data of CTS specimen CH03-01 at 60 % Cv.Le on the cutaneous side at dynamic load rate (500 mm/s) for determination of strain rates over the curve slope. Due to small rotations around the *z*-axis, the linear curve fit was applied on two sections: 30-50 % and 70-90 % of peak strain.

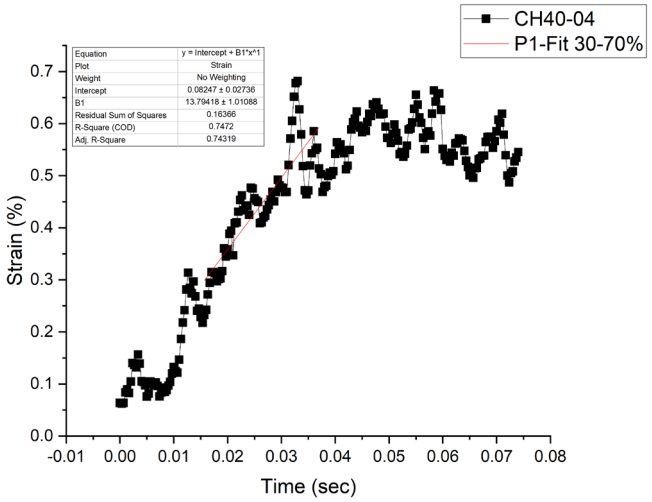

Fig. 7. Exemplary strain-time history data of EMI specimen CH40-04 at 60 % Cv.Le on the cutaneous side at dynamic load rate (500 mm/s) for determination of strain rates over the curve slope. The linear curve fit was applied on 30-70 % of peak strain.

The F-D curves (Figure 8) show a comparison of the quasi-static and dynamic tests of the CTS specimens with the dynamic tests of the EMI specimens. As a comparison to PMHS data, the F-D corridors from Kang *et al.* [28] of adult male subjects in the broad age categories (young adults (22-40 years), middle adults (41-60 years) and older adults (61+ years)) according to Agnew *et al.* [19], were added. The displacement in the *x*-direction was normalized by the original span length (Sp.Le) for the respective specimens. It is evident herein that the CTS specimens exhibit strain rate dependence that affects the structural properties and resulting maximum failure forces (q-s: (198.1 ± 7.1) N, dyn: (232.2 ± 7.3) N). Due to the strongly different material properties, geometrical differences and failure behaviour (CTS: brittle, EMI: elastic-plastic), different curve characteristics result. The CTS specimens, as with the strains, have two distinct regions (boundary between 13 % displacement) due to the initial rotation about the *z*-axis. The EMI specimens have an initial linear-elastic region (up to 4 % displacement) that quickly ends in the plastic region. Due to the necking, the resulting force decreases noticeably until about 17 % displacement. The EMI specimen peak force is (128.3 ± 6.6) N. The comparison of the CTS surrogates to the PMHS data F-D corridors [28] shows good agreement with all age groups in the lower ranges of the corridors. At a displacement of ~13 % the curve changes and leaves the F-D corridors between ~17-19 % for the dynamic and between ~18-21% for the quasi-static tests. The EMI specimens show significantly poorer to no agreement with the F-D corridors. This results from the differentiated material and failure behaviour. For further consideration and comparisons to PMHS data, only the dynamic tests are considered.

The advantage of the 3D-DIC system is evident in the study of the principal strain (absolute values) progression along the rib curve length Cv.Le (Figure 9). There is a clear difference in the strain curves on both sides of the two rib surrogates, with the maxima occurring on the anterior side (cutaneous). The side difference is much more pronounced for the CTS specimens than for the EMI specimens. The measurement range of the CTS posterior (pleural) only extends to approximately 64 % Cv.Le, as the acquisition of the measurement images was complicated by the posterior structure. The same applies to the EMI specimen posterior side. On the anterior side of the CTS samples, the maximum strain can be seen at approx. 62 % Cv.Le. This also corresponds with the fracture range. The strain profile of the EMI specimens is clearly more complex. This results from the double-curved shape of the ribs and the different cross-sections over the whole length of the curve (Cv.Le). The thickness of the cortical bone increases starting from the vertebral region up to 41 % Cv.Le and then decreases continuously, with a significant decrease from 57 % Cv.Le. The thickness of the cortical bone on the posterior side (pleural) is significantly larger than on the other sides. This results in the relatively constant strain curve on the posterior side for the EMI specimens, although significantly larger deviations were also measured here due to the measurement difficulties.

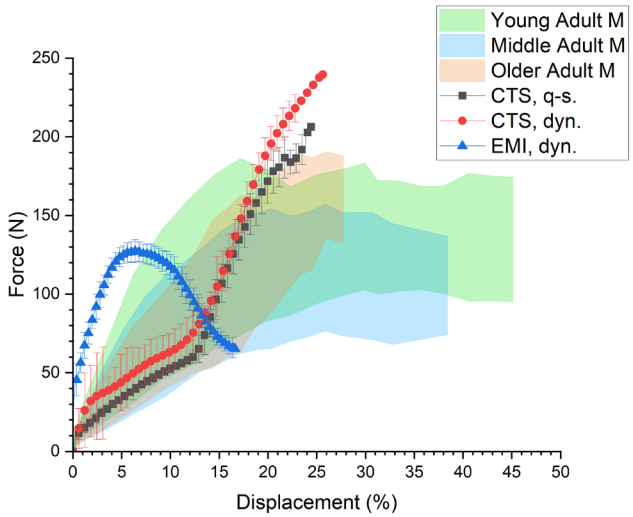

Fig. 8. F-D curves for rib surrogates CTS at quasi static (q-s.) load rate (2 mm/s), CTS and EMI at dynamic (dyn.) load rate (500 mm/s) compared to PMHS (M = male) broad age categories F-D corridors from Kang *et al.* [28].

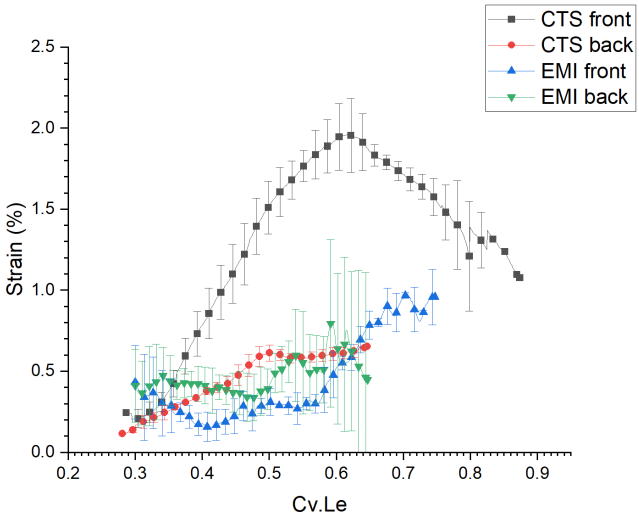

Fig. 9. Principal-strain (absolute values) rib curvature length (Cv.Le) curves for rib surrogates CTS and EMI at dynamic load rate (500 mm/s), comparison of back (posterior) and front (anterior) of the specimen.

Figure 10 shows the comparison of PMHS adult male data peak force divided into broad age categories [19], with peak force standard deviation (SD) range of rib surrogates CTS and EMI. The PMHS data are showing a slight increase during the young adult period and a subsequent decline through the other adult periods. Clearly, the CTS specimens exceed the PMHS values even in the maximum young adult region by a factor of 1.7. The EMI specimens cover a larger valid range. This includes the large range of adult males from 22 to 60 years.

The comparison of PMHS adult male data peak displacement divided into broad age categories [19] with peak displacement SD range of rib surrogates CTS and EMI is shown in Figure 11. In contrast to the peak force data, the standard deviation of the peak displacement of the EMI specimens is lower (16.08 ± 0.45) % than that of the CTS specimens (22.26 ± 1.54) %. During specimen fabrication, imperfections (grains, air inclusions) are more likely to occur during casting than in additive manufacturing. Although similar effects can occur with LBM, the repeatability is rather high and defects are very likely to be smaller in size. Nevertheless, both rib surrogates are within a valid range of the PMHS male adult data, with the CTS specimens covering a wider range from 22 to 60 years. The EMI specimens cover only a portion of the older population for 61+ years.

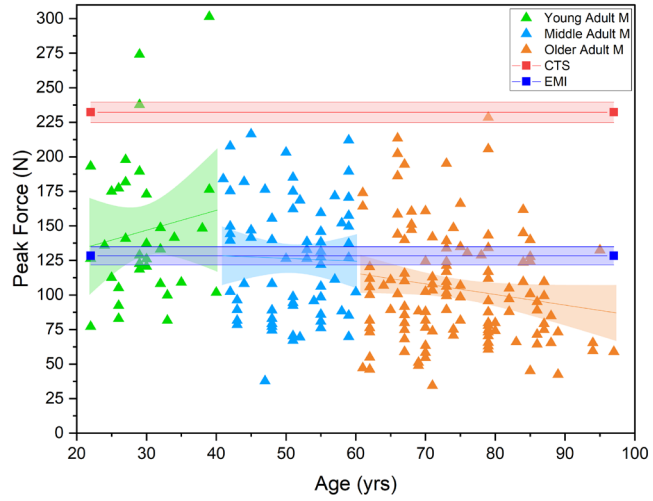

Fig. 10. Comparison of PMHS adult male data peak force divided into broad age categories [19], with peak force SD range of rib surrogates CTS and EMI at dynamic load rates (500 mm/s).

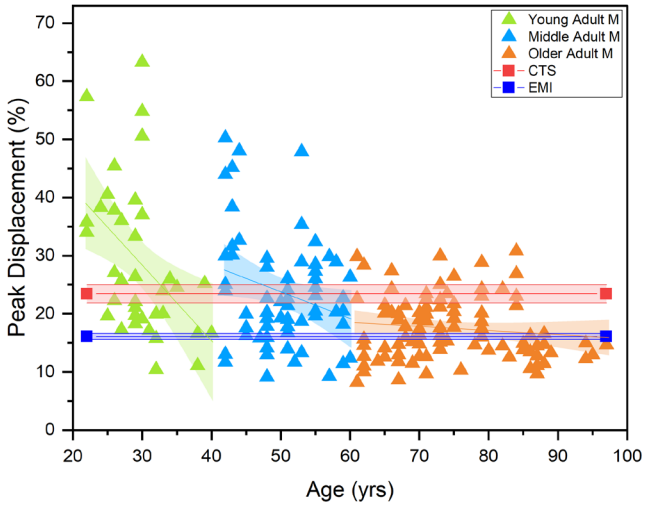

Fig. 11. Comparison of PMHS adult male data peak displacement divided into broad age categories [19], with peak displacement SD range of rib surrogates CTS and EMI at dynamic load rate (500 mm/sec).

Figures 12 and 13 show the boxplot comparison of the CTS and EMI rib surrogates to the peak force and peak displacement to PMHS male data by specific age category. In addition to the PMHS data from Agnew *et al.* [19], the data from Kang *et al.* [28] were used for comparison since they are also available in the same age categories. One should note that the data from [28] are given only as mean with standard deviation. The PMHS data correspond well in their mean values, with both parameters deviating the most in the young adult group. This could result from the relatively narrow range of data that was used to generate the results. The dispersion value of the boxplot (interquartile range) is also in good agreement with the standard deviation of the corresponding PMHS data. It is clear that the CTS specimens have significantly higher peak forces and cannot be associated with any age category (if applicable, only with the outlier values). The EMI specimens are in good agreement with the young adult male and in the upper range of the middle adult male group. For the peak displacement, the CTS specimens are in good agreement with young adult male and middle adult male group. The EMI specimens are in the mid-range of the older adult group.

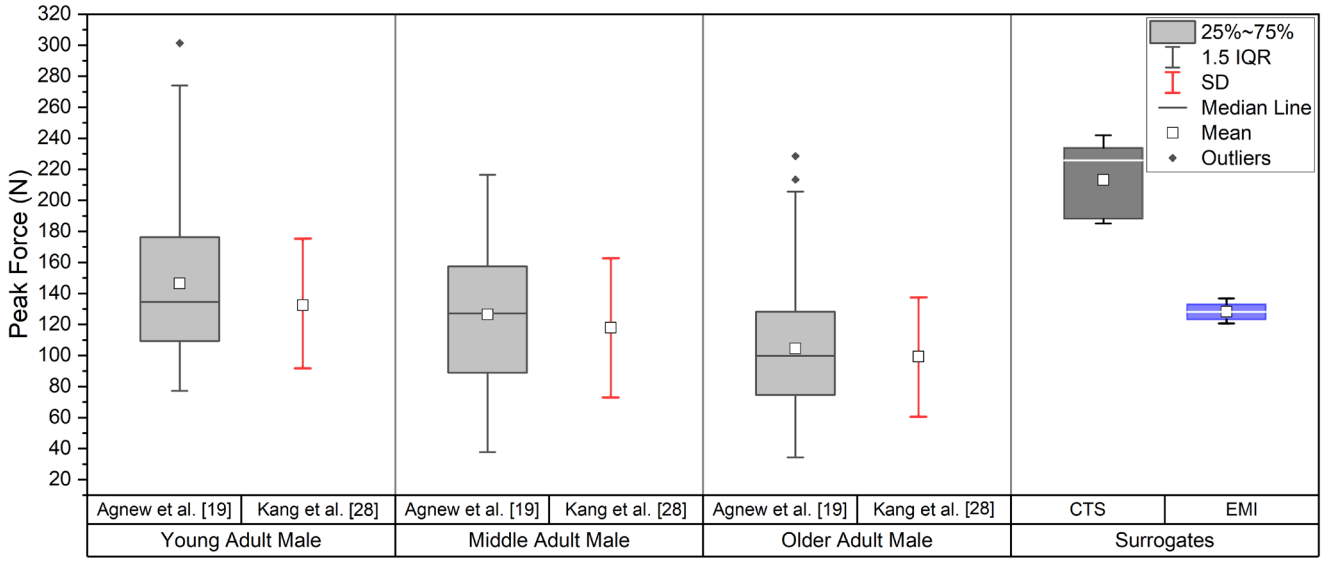

Fig. 12. Comparison of PMHS data peak force by specific age category from [19] and [28] (only mean ± SD), with peak force of rib surrogates CTS and EMI at dynamic load rate (500 mm/s).

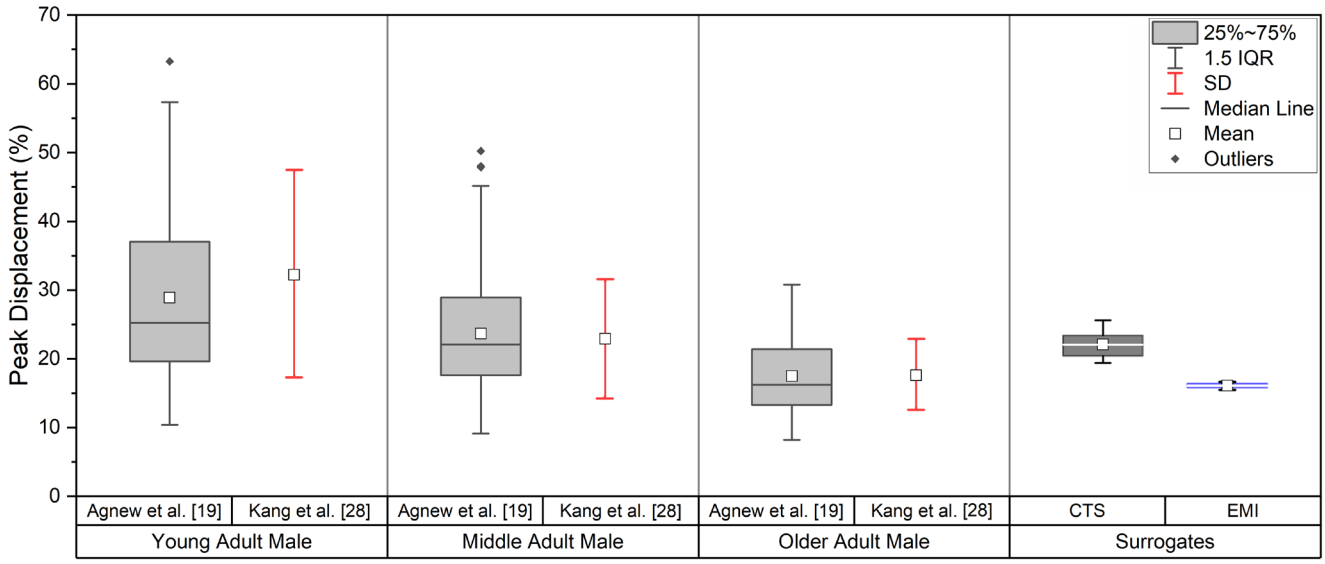

Fig. 13. Comparison of PMHS data peak displacement by specific age category from [19] and [28] (only mean ± SD), with peak force of rib surrogates CTS and EMI at dynamic load rate (500 mm/s).

All characteristic structural properties of the surrogates and the PMHS data are summarized in Table VI. Additionally to the peak force and peak displacement data, the maximum compressive strains at 60 % Cv.Le on the cutaneous side and the stiffness *K* of the specimens are compared. Since Kindig [26] used different measurement positions for the strains, the stated value was acquired at around 52 % Cv.Le. Nevertheless, the value is in good agreement with the corresponding PMHS data. As can be seen, the CTS specimens achieved almost twice the strain and the EMI specimens only nearly half the strain of the comparative values. For the stiffness *K*, both surrogates have even larger deviations (the CTS samples nearly triple and the EMI samples more than five times the reference values).

TABLE VI
COMPARISON OF STRUCTURAL PROPERTIES OF RIB BONE SURROGATES WITH PMHS DATA

	Peak Force (N)	**Peak Displacement (%)**	**Peak Comp. Strain @60 % Cv.Le (%)**	**Stiffness *K* (N/mm)**
CTS	232.2 ± 7.3	23.4 ± 1.6	1.86 ± 0.10	7.64 ± 0.76
EMI	128.3 ± 6.6	16.1 ± 0.4	0.57 ± 0.03	13.19 ± 1.10
PMHS male 5th rib [24]	98.3 ± 36.9	19.8 ± 4.6	1.11 ± 0.19	2.59 ± 0.98
PMHS male 5th rib [26]	82.5 ± 18.3	27.8 ± 6.1	1.02 ± 0.18	2.25 ± 0.52
PMHS male 3th–8th rib lv. [19]	116.2 ± 46.6	22.8 ± 10.6	1.27 ± 0.66	3.92 ± 1.75
PMHS mid-size male 4th–7th rib lv. [28]	114.6 ± 41.4	22.9 ± 9.4	N/A	N/A

IV. DISCUSSION

The objective of this study was to compare the CTS PRIMUS breakable dummies and their bone structures, explicitly the ribs, which are already used in the traffic accident research, with PMHS characteristic values from the literature. In addition, the aim was to present a new possibility of production (additive manufacturing) in the field of fabrication methods of rib surrogates, and also to compare them with PMHS data from literature [19][24][26][28]. Since the geometry of female ribs is very different from that of a male PMHS, which was used as a template in this study, only the characteristic values assigned to males will be considered for further adjustments, where possible. The analysis of female ribs should be addressed in a separate study.

The test boundary conditions differed from the PMHS test in some particulars: potted rib ends geometrical conditions are different because the clamping device is designed otherwise, vertebral end fixed (no rotation about *z*-axis), test velocity (dynamic) 500 mm/s, [19] 2000 mm/s, [24] 1750 mm/s, [26] 500-1000 mm/s, in [28] the same device is used as in [19]. Nevertheless, the loading direction and force application to the specimens were complied with [19][24][26].

The comparative structural parameters force, displacement and strain were measured directly during the experiments, whereby the last was acquired by the three-dimensional digital image correlation (3D-DIC) method. A major advantage of this technique over conventional strain gauges is the ability to measure the strain field over the visible surface and not only at specific points of interest. In contrast to the literature, here the strain field of the specimens could additionally be recorded along the visible range and plotted over the visible course of the Cv.Le rib curve length. This allowed the localization of the largest strain regions of the specimens and a correlation to the cross-sectional geometry could be established. In comparable experiments with PMHS specimens [19][24][26][28] the strains are measured at the points 30 % and 60 % of Cv.Le. The presented results show that in the EMI rib surrogates the peak strains occur at 70-75 % of the Cv.Le and it suggests that this fact is also true for PMHS specimens, from which the cross-section geometry was taken 1:1. Nevertheless, the determined characteristic values must be considered with care, as the measurement of the strain fields strongly depends on the visible surface and the applied speckle pattern. Limits have been shown here in the posterior area of the ribs (pleural) due to the more difficult geometry. The measured strain characteristics are subject to a large scatter in this case. The measurement data of the anterior side (cutaneous) are consistent again and the scatter is acceptable for the comparisons to PMHS data. Due to the wider area of the anterior and posterior sides of the CTS specimens, there were no limitations in the measurements.

The failure behaviour of the two rib surrogates is very different. The CTS ribs behave in a brittle manner and resemble that of a real rib. The EMI surrogates, on the other hand, are elastic-plastic, which is far from the real

fracture behaviour. Furthermore, it can be assumed that the geometric differences of the CTS rib compared to the human rib influence the structural properties (deviating strain progression and stiffness). The significantly lower Young's modulus is also a factor of concern. However, these show good F-D behaviour and could be improved by changing the mold shape. The EMI rib, while accurately replicating the cross-sections and external geometry, has significantly different material properties which results also in deviating strain progression and stiffness. Despite this, peak force and peak displacement are in good agreement, but F-D progression is too inconsistent with PMHS data. A different additive manufacturing material might be preferable. The current one was chosen due to the high precision of the process. The thin cross-sections cannot be realized with other materials. Further studies are intended to better investigate this issue. By increasing the wall thickness of the surrogate, a different cross-section is implemented compared to the real rib. However, this opens up new possibilities for parameter variation in additive manufacturing and a more brittle fracture behaviour could be realized.

It is assumed that due to a slight rotation of the mount around the *z*-axis at the sternal end, two different strain rates are obtained for the CTS specimens because the initial distortion resulted in the force being not completely introduced into the specimen. In addition, the lower test velocity may have increased the effect. In the pendulum test rig as in [19] and [24], the specimens are tested at up to 2000 mm/s. An initial slight rotation probably does not have such a large influence on the strain rate. Also, the already discussed different boundary conditions could have an influence.

V. CONCLUSIONS

The comparison of the CTS specimens to the PMHS characteristic values has shown good agreements, but also differences. The determined characteristic values of the peak forces, the corresponding peak strains and stiffness were considerable higher than the reference values. In contrast, the F-D curve behaviour of the CTS specimens shows good agreement with PMHS male data and covers the range of young and middle adult age groups. It is recommended to adjust the mixing ratio of epoxy resin and aluminium powder. In order to achieve the young adult male values targeted by the designers and manufacturers, the maximum force must be significantly reduced and the peak strains slightly reduced. This could be achieved by increasing the aluminium powder content, as this would make the final material more brittle. In addition, the cross-section could be reduced in the 30-80 % Cv.Le ranges to more closely approximate that of a realistic rib, thereby reducing the ultimate strength without significantly changing the strain behaviour.

The comparison of the EMI specimens to the PMHS characteristics found good agreement in some areas, but has also shown the disadvantages of the material. The peak forces could be assigned to the age groups young and middle adult males. The peak strains obtained were more in the intermediate range of middle-aged and older adults and the corresponding peak displacements were in the older adult male range. For the further development of the EMI rib surrogates, a significantly less ductile response must be achieved in order to convert the linear-elastic characteristic behaviour into a brittle response and to eliminate the plastic behaviour as far as possible.

VI. REFERENCES

[1] Kent, R., Woods, W., Bostrom, O. (2008) Fatality risk and the presence of rib fractures. *Annals of Advances in Automotive Medicine*, **52**: pp.73–84.

[2] Page, Y., Cuny, S., Hermitte, T., Labrousse, M. (2012) A comprehensive overview of the frequency and the severity of injuries sustained by car occupants and subsequent implications in terms of injury prevention. *Annals of Advances in Automotive Medicine*, **56**: pp.165–174.

[3] Weaver, A. A., Talton, J. W., *et al*. (2015) Estimated injury risk for specific injuries and body regions in frontal motor vehicle crashes. *Traffic Injury Prevention*, **16**: pp.108–116.

[4] Kent, R., Henary, B., Matsuoka, F. (2005) On the fatal crash experience of older drivers. *Annals of Advances in Automotive Medicine*, **49**: pp.371–391.

[5] Lien, Y., Chen, C., Lin, H. (2009) Risk factors for 24-hour mortality after traumatic rib fractures owing to motor vehicle accidents: A nationwide population-based study. *Annals of Thoracic Surgery*, **88**: pp.1124–1130.

[6] Duma, S. M., Kemper, A. R., *et al*. (2011) Rib Fracture Timing in Dynamic Belt Tests with Human Cadavers. *Clinical Anatomy*, **24**: pp.327–338.

[7] Forman, J., Poplin, G. S., *et al*. (2019) Automobile injury trends in the contemporary fleet: belted occupants in frontal collisions. *Traffic Injury Prevention*, **20**: pp.607–612.
[8] Collins, J. (2000) Chest Wall Trauma. *Journal of Thoracic Imaging*, **15**: pp.112-119.
[9] Lee, E., Craig, M., and Scarboro, M. (2015) Real-world rib fracture patterns in frontal crashes in different restraint conditions. *Traffic Injury Prevention*, **16**: pp.115-S123.
[10] Novakov, I., Timonov, P., Stefanov, C., Petkov, G. (2014) Rib fractures in blunt chest trauma-morbidity and mortality: Self-experience study. *Trakia Journal of Sciences*, **12**: pp.272-276.
[11] Holcomb, J. B., McMullin, N. R., Kozar, R. A., Lygas, M. H., Moore, F. A. (2003) Morbidity from rib fractures increases after age 45. *Journal of the American College of Surgeons*, **196**: pp.549–555.
[12] Brumbelow, M. L. (2019) Front crash injury risks for restrained drivers in good-rated vehicles by age, impact configuration, and EDR-based delta V. *Proceedings of the International Research Council on Biomechanics of Injury*, 2019, Florence, Italy.
[13] Kemper, A. R., McNally, C., *et al*. (2005) Material properties of human rib cortical bone from dynamic tension coupon testing. *Stapp Car Crash Journal*, **49**: pp.199–230.
[14] Stitzel, J., Kilgo, P., *et al*. (2010) Age thresholds for increased mortality of predominant crash induced thoracic injuries. *Annals of the Advancement of Automotive Medicine*, **54**: pp.41–50.
[15] Katzenberger, M. J., Albert, D. L., Agnew, A. M., Kemper, A. R. (2020) Effects of sex, age, and two loading rates on the tensile material properties of human rib cortical bone. *Journal of the Mechanical Behavior of Biomedical Materials*, **102**: 103410.
[16] Mayeur, O., Chaari, F., Delille, R., Drazetic, P., Markiewicz, E. (2012) Analysis of the cortical bone thickness of human thorax based on multi-scale imaging techniques. *Computer Methods in Biomechanics and Biomedical Engineering*, **15**: pp.279–280.
[17] Kalra, A., Saif, T., *et al*. (2015) Characterization of human rib biomechanical response due to three-point bending. *Stapp Car Crash Journal*, **59**: pp.113–130.
[18] Agnew, A., Murach, M., *et al.* (2017) The effect of body size on adult human rib structural properties. *Proceedings of the International Research Council on Biomechanics of Injury*, 2017, Antwerp, Belgium.
[19] Agnew, A., Murach, M., *et al*. (2018) Sources of Variability in Structural Bending Response of Pediatric and Adult Human Ribs in Dynamic Frontal Impacts. *Stapp Car Crash Journal*, **62**: pp.119–192.
[20] Velazquez-Ameijidea, J., Garcia-Vilanaa, S., *et al*. (2021) Influence of anthopometric variables on the mechanical properties of human rib cortical bone. *Biomedical Physics & Engineering Express*, **7**: 035013.
[21] Knets, I., Melnis, A., Dobelis, M. (1999) Effect of Time Dependence on the Mechanical Behavior of Compact Bone Tissue. *Proceedings of IUTAM Symposium on Synthesis in Bio Solid Mechanics*, 1999, Dordrecht Netherlands.
[22] Hansen, U., Zioupos, P., Simpson, R., Currey, J., Hynd, D. (2008) The effect of strain rate on the mechanical properties of human cortical bone. *Journal of Biomechanical Engineering*, **130**:011011.
[23] Roberts, S. B., Chen, P. (1972) Global geometric characteristics of typical human ribs. *Journal of Biomechanics*, **5**: pp.191–201.
[24] Charpail, E., Trosseille, X., *et al.* (2005) Characterization of PMHS Ribs: A new Test Methodology. *Stapp Car Crash Journal*, **49**: pp.183–198.
[25] Charpail, E., Laporte, S., Trosseille, X., Valancien, G., Lavaste, F. (2005) Material and Structure Characterization of Human Ribs. *Journal of Biomechanics*, **39**: pp.55–S156.
[26] Kindig, M. (2009) Tolerance to Failure and Geometric Influences on the Stiffness of Human Ribs Under Anterior-posterior Loading. *University of Virginia*, 2009, Charlottesville, United States.
[27] Murach, M., Bazyk, A., *et al*. (2016) Utilization of a novel method for measuring cortical thickness to investigate variation with age in male human ribs. *Proceedings of the International Research Council on Biomechanics of Injury*, 2016, Malaga, Spain.
[28] Kang, Y., Kwon, H., Stammen, J., Moorhouse, K., Agnew, A. (2020). Biomechanical Response Targets of Adult Human Ribs in Frontal Impacts. *Annals of Biomedical Engineering*, **49**: pp.900-911.
[29] White, R. P., Rangarajan, N., Haffner, M. (1996) Development of the THOR Advanced Frontal Crash Test Dummy. *Proceedings of the SAFE Conference*, 1996, Vienna, Austria.
[30] Rangarajan, N., White, R., *et al*. (1998) Design Criteria, Design, and Performance of the THOR Advanced Frontal Crash Test Dummy Thorax and Abdomen assemblies. *Proceedings of the 16th International Technical Conference on the Enhanced Safety of Vehicles (ESV)*, 1998, Ontario, Canada.
[31] Weyde, M. (2016) Anwendbarkeit von Dummy-Versuchen in der forensischen Praxis bei der Rekonstruktion von Pkw-Fußgänger-Unfällen. *Wildhaus: AREC Group*, 2016.

[32] Hartwig, S., Knape, M., Kunze, A., Weyde, M. (2017) Interdisziplinäre Weiterentwicklung eines optimierten biofidelen Dummys als Fußgänger-Surrogat bei Full-Scale Crashtests. *Proceedings of EVU-Tagung*, 2017, Haarlem, Netherlands.

[33] Härtel, B., Hannawald, L. (2019) Research and development of a new biofidelic dummy. *Proceedings of the 28th European Association for Accident Research and Analysis (EVU) Conference*, 2019, Barcelona, Spain.

[34] Schäuble, A., Weyde, M. (2019) Biomechanical Validation of a New Biofidelic Dummy. *NHTSA 26th ESV*, 2019.

[35] Yan, C., Hao, L., Hussein, A., Young, P. (2015) Ti-6Al-4V triply periodic minimal surface structures for bone implants fabricated via selective laser melting. *Journal of the Mechanical Behavior of Biomedical Materials*, **51**: pp.61–73.

[36] Wang, X., Xu, S., *et al*. (2016) Topological design and additive manufacturing of porous metals for bone scaffolds and orthopaedic implants: A review. *Biomaterials*, **83**: pp.127–141.

[37] Shi, J., Liang, H., Jiang, J., Tang, W., Yang, J. (2019) Design and Performance Evaluation of Porous Titanium Alloy Structures for Bone Implantation. *Mathematical Problems in Engineering*, 2019, ID 5268280.

[38] Majmoud, D., Elbestawi, M. A. (2019) Selective laser melting of porosity graded lattice structures for bone implants. *The International Journal of Advanced Manufacturing Technology*, **100**: pp.2915–2927.

[39] Hoschke, K., Pfaff, A., *et al*. (2018) A parametric mesostructural approach for robust design of additive manufacturing parts. *Proceedings of Fraunhofer Direct Digital Manufacturing Conference (DDMC)*, 2018, Berlin, Germany.

[40] Pfaff, A., Jäcklein, M., Hoschke, K., Wickert, M. (2018) LBM Process Parameter Optimization for Designed Materials. *Proceedings of Fraunhofer Direct Digital Manufacturing Conference (DDMC)*, 2018, Berlin, Germany.

[41] Jäcklein, M., Pfaff, A., Bierdel, M., Hoschke, K., Wickert, M. (2018) Micro- and Macrostructural Investigations of AlSi10Mg Produced by Laser Beam Melting. *Proceedings of Fraunhofer Direct Digital Manufacturing Conference (DDMC)*, 2018, Berlin, Germany.

[42] Jakkula, P., Ganzenmüller, G., *et al*. (2021) Strain Rate Sensitivity of the Additive Manufacturing Material Scalmalloy®. *Journal of Dynamic Behavior of Materials*, **7**: pp.518–525.

[43] "Material data sheet for steel parts produced by Laser Melting (PBF-LB/M) - SCALMALLOY®" Internet: [https://fit.technology/downloads/pdf/Materialdatasheet_Metal_LM_FIT.pdf], Version 1.4 / February 2021.

[44] Kortmann, A. (2018) Crashverhalten im Crashvergleich: der neue Biofidel-Dummy bei unterschiedlichen Szenarien von Pkw-Fußgängerunfällen. *VKU Verkehrsunfall und Fahrzeugtechnik*, **03**: pp.102–112.

[45] Gayzik, F. S., Moreno, D. P., *et al*. (2011) Development of a Full Body CAD Dataset for Computational Modeling: A Multi-modality Approach. *Annals of Biomedical Engineering*, **39**: pp.2568–2583.

[46] Grindle, D., Pak, W., *et al*. (2021) A detailed finite element model of a mid-sized male for the investigation of traffic pedestrian accidents. *Proceedings of the Institution of Mechanical Engineers, Part H: Journal of engineering in medicine*, **235.3**: pp.300–313.

[47] Kindig, M., Lau, A. G., Kent, R. W. (2011) Biomechanical Response of Ribs Under Quasistatic Frontal Loading. *Traffic Injury Prevention*, **12**: pp.377–387.